Quantifying Spin-Orbit Torques in Antiferromagnet–Heavy-Metal Heterostructures

Egecan Cogulu,[1] Hantao Zhang,[2] Nahuel N. Statuto,[1] Yang Cheng,[3] Fengyuan Yang,[3] Ran Cheng,[2,4] and Andrew D. Kent[1]

[1]Center for Quantum Phenomena, Department of Physics, New York University, New York 10003, USA
[2]Department of Electrical and Computer Engineering, University of California, Riverside, California 92521, USA
[3]Department of Physics, The Ohio State University, Columbus, Ohio 43210, USA
[4]Department of Physics and Astronomy, University of California, Riverside, California 92521, USA

(Received 20 December 2021; accepted 2 June 2022; published 17 June 2022)

The effect of spin currents on the magnetic order of insulating antiferromagnets (AFMs) is of fundamental interest and can enable new applications. Toward this goal, characterizing the spin-orbit torques (SOTs) associated with AFM–heavy-metal (HM) interfaces is important. Here we report the full angular dependence of the harmonic Hall voltages in a predominantly easy-plane AFM, epitaxial c-axis oriented α-Fe_2O_3 films, with an interface to Pt. By modeling the harmonic Hall signals together with the α-Fe_2O_3 magnetic parameters, we determine the amplitudes of fieldlike and dampinglike SOTs. Out-of-plane field scans are shown to be essential to determining the dampinglike component of the torques. In contrast to ferromagnetic–heavy-metal heterostructures, our results demonstrate that the fieldlike torques are significantly larger than the dampinglike torques, which we correlate with the presence of a large imaginary component of the interface spin-mixing conductance. Our work demonstrates a direct way of characterizing SOTs in AFM-HM heterostructures.

DOI: 10.1103/PhysRevLett.128.247204

Recently antiferromagnetic materials have been gathering increasing attention from the spintronics community due to their advantageous properties such as fast spin dynamics, low susceptibility, and magnetic moment compensation [1–4]. Detecting and manipulating antiferromagnetic order electrically is an important milestone for realizing devices based on AFMs [5–9]. It is known that spin-orbit torques (SOTs) are one of the most effective ways to manipulate magnetic order in both ferromagnets (FMs) and ferrimagnets [10–18]. However, their effectiveness is less well explored and quantified for AFMs. Therefore, characterizing the SOTs is crucial for understanding and predicting AFM dynamics. A powerful technique to characterize SOTs is harmonic Hall measurements [19,20]. Although this technique has been used extensively in FM–heavy-metal (HM) bilayers, harmonic Hall study of SOTs in AFMs remains elusive.

In this work, we use harmonic Hall measurements to characterize the SOTs in α-Fe_2O_3/Pt bilayers. SOTs are a result of the spin-Hall effect (SHE) in Pt [21,22], in which a charge current leads to a spin accumulation at the α-Fe_2O_3 interface. SOTs can modify the orientation of the AFM Néel vector and this change can be detected electrically because of spin Hall magnetoresistance (SMR) [23,24]. SMR arises from the combination of the SHE, interface scattering, and the inverse SHE [25]. Most importantly for our study, SMR manifests as an anisotropy in the resistivity of the Pt and a Hall signal analogous to the planar Hall in ferromagnets [26]. We first characterize the SMR by the first harmonic response and then SOTs from the second harmonic response.

Then, we develop a model of the response that accounts for the magnetic properties of α-Fe_2O_3 and compare the model with the experimental results. By fitting the data from six measurements together (the first and second harmonic response with the field rotated in three orthogonal planes), we extract the amplitudes of the dampinglike and fieldlike torques. Surprisingly and contrary to the case of ferromagnet–heavy-metal heterostructures, we find fieldlike torques to be significantly larger than dampinglike torques.

Figure 1(a) shows a schematic of the experimental setup. We perform Hall measurements at 300 K on 30 nm thick epitaxial c-axis oriented α-Fe_2O_3 on Al_2O_3 (0001) substrates capped *in situ* with 5 nm thick Pt [8,20]. The Pt layer is patterned into a 5×15 μm^2 Hall-cross structure and the Hall voltage is detected with a lock-in amplifier with a 953 Hz ac current of 4×10^9 A/m^2 and 6×10^{10} A/m^2 used for first and second harmonic measurements, respectively.

Figure 1(b) shows the geometry used in our model. The antiferromagnet's hard axis and Dzyaloshinskii-Moriya interactions (DMI) vector are represented by the same vector $\boldsymbol{D}$. The AFM sublattice moment directions are indicated by unit vectors $\boldsymbol{m}_1$ and $\boldsymbol{m}_2$. The Néel vector $\boldsymbol{n} = (\boldsymbol{m}_1 - \boldsymbol{m}_2)/2$ lies in the easy plane, which is perpendicular to $\boldsymbol{D}$, indicated by the red plane. $\boldsymbol{H}$ is the applied magnetic field and $\boldsymbol{\sigma}_{ac}$ is the spin accumulation at the interface caused

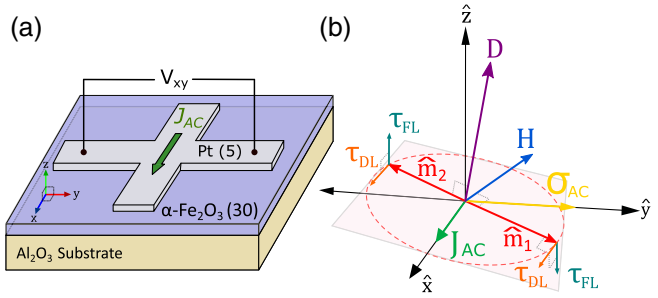

FIG. 1. (a) Transverse measurement configuration showing the Pt Hall cross with 5 μm channel width. An ac current $\boldsymbol{J}_{\rm ac}$ is applied in the $\hat{x}$ direction, and the transverse voltage V_{xy} is measured with a lock-in amplifier. (b) Modeling geometry. $\boldsymbol{D}$ represents both the DMI vector and the hard axis direction that defines the easy plane. $\boldsymbol{m}_1$ and $\boldsymbol{m}_2$ are the sublattice moments and $\boldsymbol{H}$ is the external magnetic field. The spin accumulation $\boldsymbol{\sigma}_{\rm ac}$ is in the $\hat{y}$ direction. The resulting spin-orbit torques on the sublattice moments are decomposed into fieldlike ($\tau_{\rm FL}$) and dampinglike components ($\tau_{\rm DL}$).

by $\boldsymbol{J}_{\rm ac}$ via the SHE. The resulting SOTs on the sublattice moments are decomposed into fieldlike ($\tau_{\rm FL}$) and dampinglike components ($\tau_{\rm DL}$). Notice we do not constrain $\boldsymbol{D}$ to be parallel to the $\hat{z}$ axis, as canting of the easy plane in AFMs, due to the strain effects from the substrate, has been reported [9,27]. As shown at the top of Fig. 2, $\boldsymbol{H}$ is rotated in one of the three planes: XY, XZ, or YZ, where the current $\boldsymbol{J}_{\rm ac}$ is in the $\hat{x}$ direction.

Figure 2 shows the full angular dependence of Hall signals (blue points), for all three field scans, at $\mu_0 H = 3$ T together with the model fit (red lines). In the in-plane XY scan, both first and second harmonic Hall signals follow smooth trigonometric functions. This is expected because SMR and fieldlike torques are the main contributors in first and second XY scan harmonic signals, respectively. On the other hand, for out-of-plane field rotation experiments —XZ and YZ field scans—the angular dependencies do not follow a simple trigonometric function. A comprehensive model is needed in order to explain all six scans, as we discuss below.

In the sample geometry indicated in Fig. 1(b), an ac current density $J_{\rm ac}(t) = J_0 \cos\omega t$ generates an oscillating spin accumulation $\sigma_{\rm ac}(t)$ in the $\hat{y}$ direction, which produces SOTs on α-Fe_2O_3. The measured Hall voltage V_{xy} arises from the SMR: $V_{xy}(t) = A_x J_0 R_{xy}[\boldsymbol{n}(J_{\rm ac}, \boldsymbol{H})] \cos\omega t$, where A_x is the area through which the current flows and R_{xy} has the form $R_{xy} \sim n_x n_y$ [25,29–32]. Since the current-induced torques only result in a slight deviation of $\boldsymbol{n}$ from its equilibrium orientation, we can expand the SMR as

$$R_{xy}[\boldsymbol{n}(J_{\rm ac}, \boldsymbol{H})] = R_{xy}[\boldsymbol{n}(0, \boldsymbol{H})] + J_0 \left(\frac{\partial R_{xy}}{\partial \boldsymbol{n}}\right) \frac{\partial \boldsymbol{n}}{\partial J_{\rm ac}}\bigg|_{(0,\boldsymbol{H})} \cos\omega t + h.o., \quad (1)$$

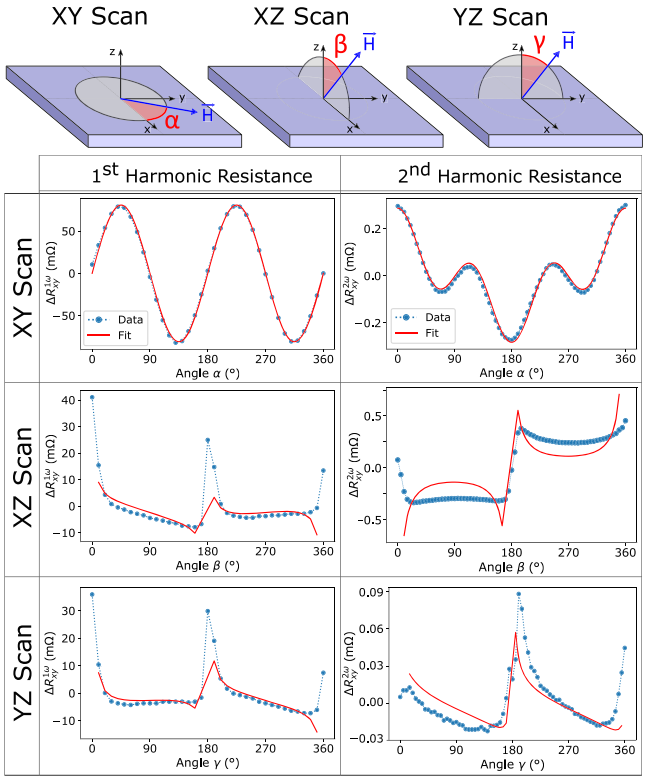

FIG. 2. Angular dependence of first and second harmonic (columns) resistance signals in XY, XZ, and YZ scans (rows) at $\mu_0 H = 3$ T. The current amplitudes are 100 μA and 1.5 mA in the first and second harmonic measurements, respectively. The blue dots are the data points whereas, the red line is the fit resulting from our model that is described in the main text. The geometry of magnetic field scans in the three principal planes (XY, XZ, and YZ scans) and the definition of the angles α, β, and γ are shown at the top. The magnitude of longitudinal SMR is approximately 0.02% and it is consistent with studies on similar AFM-HM systems [24,28].

where the first term $R_{xy}[\boldsymbol{n}(0, \boldsymbol{H})]$ is the SMR, which leads to the first harmonic signal $V_{xy}^{1\omega}(t) = A_x J_0 R_{xy}[\boldsymbol{n}(0, \boldsymbol{H})] \cos\omega t$. The second term, which is itself proportional to J_0, gives rise to the second harmonic response $V_{xy}^{2\omega}(t)$. Therefore, to find the harmonic responses, we need to calculate $\boldsymbol{n}(0, \boldsymbol{H})$. $\partial \boldsymbol{n}/\partial J_{\rm ac}$ is determined by the dynamics of the Néel vector and hence by the dynamics of sublattice magnetic moments, $\boldsymbol{m}_1$ and $\boldsymbol{m}_2$.

In the macrospin approximation, the free energy density (in field dimensions of Tesla) can be expressed as

$$\frac{\epsilon}{\hbar\gamma} = H_{\rm ex} \boldsymbol{m}_1 \cdot \boldsymbol{m}_2 + H_K[(\boldsymbol{e}_h \cdot \boldsymbol{m}_1)^2 + (\boldsymbol{e}_h \cdot \boldsymbol{m}_2)^2] - H_D \boldsymbol{e}_D \cdot (\boldsymbol{m}_1 \times \boldsymbol{m}_2) - \boldsymbol{H} \cdot (\boldsymbol{m}_1 + \boldsymbol{m}_2), \quad (2)$$

where γ is the gyromagnetic ratio. $\boldsymbol{e}_h$ and $\boldsymbol{e}_D$ are unit vectors in the directions of the hard axis anisotropy and DMI, respectively. $H_{\rm ex}$, H_K, and H_D are the effective fields

associated with the exchange interaction, the hard axis anisotropy, and the DMI, respectively. Here we have ignored the in-plane easy axis anisotropy because it is much weaker than H_K and H_D [31]. This simplification, however, becomes invalid when the in-plane projection of $\boldsymbol{H}$ is insufficient to maintain a single domain state [20] (e.g., when $\boldsymbol{H}$ is nearly perpendicular to the easy plane). The dynamics of the sublattice magnetic moments are described by the coupled Landau-Lifshitz-Gilbert-Slonczewski equations:

$$\frac{d\boldsymbol{m}_{1,2}}{dt} = \gamma \boldsymbol{H}_{1,2}^{\mathrm{eff}} \times \boldsymbol{m}_{1,2} + \alpha_0 \boldsymbol{m}_{1,2} \times \frac{d\boldsymbol{m}_{1,2}}{dt} + \gamma[H_{\mathrm{Oe}}(J_{\mathrm{ac}}) + H_{\mathrm{FL}}(J_{\mathrm{ac}})]\boldsymbol{\sigma}_{\mathrm{ac}} \times \boldsymbol{m}_{1,2} + \gamma H_{\mathrm{DL}}(J_{\mathrm{ac}})\boldsymbol{m}_{1,2} \times [\boldsymbol{m}_{1,2} \times \boldsymbol{\sigma}_{\mathrm{ac}}], \quad (3)$$

where $\boldsymbol{H}_{1,2}^{\mathrm{eff}} = -\delta\epsilon/(\hbar\gamma\delta\boldsymbol{m}_{1,2})$ is the effective field acting on $\boldsymbol{m}_{1,2}$, α_0 is the Gilbert damping constant, $H_{\mathrm{Oe}}(J_{\mathrm{ac}}) = \frac{1}{2}\mu_0 A_x J_{\mathrm{ac}} t_{\mathrm{Pt}}$ is the Oersted field, and t_{Pt} the thickness of the Pt film. $\boldsymbol{\sigma}_{\mathrm{ac}}$ is the direction of spin accumulation (here along $\hat{y}$), and $H_{\mathrm{FL}}(J_{\mathrm{ac}})$ and $H_{\mathrm{DL}}(J_{\mathrm{ac}})$ are the strengths of the fieldlike and dampinglike torques, respectively.

All the three fields generated by the current are linearly proportional to J_{ac}. In particular, H_{Oe} and H_{FL} satisfy the same symmetry, but we show that Oersted field contribution is much smaller than fieldlike SOTs, using finite-element simulations (see Supplemental Material [33]). Because the intrinsic frequency of the spin dynamics in α-Fe_2O_3 is many orders of magnitude larger than ω [34], we can treat $\boldsymbol{m}_{1,2}$ as quasistatic vectors that adiabatically adjust to the ac current, remaining in the instantaneous ground state in the presence of current-induced torques. Under the adiabatic approximation, Eq. (3) can be solved analytically [35], and, if $|\boldsymbol{m}| = |\boldsymbol{m}_1 + \boldsymbol{m}_2| \ll 1$, can be expressed by the Néel vector $\boldsymbol{n}$ as a function of J_{ac} and $\boldsymbol{H}$. Finally, by inserting $\boldsymbol{n}(J_{\mathrm{ac}}, \boldsymbol{H})$ into Eq. (1), we obtain the general solution for the SMR and thus $V_{xy}^{1\omega}$ and $V_{xy}^{2\omega}$. This general solution, however, cannot be recast into a concise form unless we assume that $\boldsymbol{e}_h \| \hat{z}$ and $\boldsymbol{e}_D \| \hat{z}$, i.e., the easy plane coincides with the film plane without tilting. The special solution for vanishing tilt is

$$R_{xy}^{1\omega} = -\frac{1}{2} R_0 \sin 2\phi_H, \quad (4)$$

$$R_{xy}^{2\omega} = R_0 \left[-\frac{\cos 2\phi_H \cos \phi_H}{H \sin \theta_H}(H_{\mathrm{Oe}} + H_{\mathrm{FL}}) + \frac{2H_{\mathrm{ex}} H \cos\theta_H \cos 2\phi_H \sin \phi_H H_{\mathrm{DL}}}{2({H_D}^2 + 2H_{\mathrm{ex}}H_K)H \sin\theta_H + H_D(H^2 + 4H_{\mathrm{ex}}H_K + {H_D}^2)} \right], \quad (5)$$

where $\theta_H \in [0, \pi]$ and $\phi_H \in [0, 2\pi]$ are the polar and azimuthal angles of $\boldsymbol{H}$, and R_0 is a current-independent constant. In Fig. 2, we identify these angles as $\theta_H = \pi/2$ and $\phi_H = \alpha$ for the XY scan, $\theta_H = \beta$ (or $2\pi - \beta$) and $\phi_H = 0$ (or π) for the XZ scan, and $\theta_H = \gamma$ (or $2\pi - \gamma$) and $\phi_H = \pi/2$ (or $3\pi/2$) for the YZ scan, respectively. To better fit the data in Fig. 2, however, we further allow a small tilting of the hard axis but still assume that $\boldsymbol{e}_D \| \boldsymbol{e}_h$, which yields a complicated expression not shown here. We observe a good agreement with the experiment at a tilt angle of $\sim 3°$ with respect to $\hat{z}$, which is plotted by the red curves in Fig. 2.

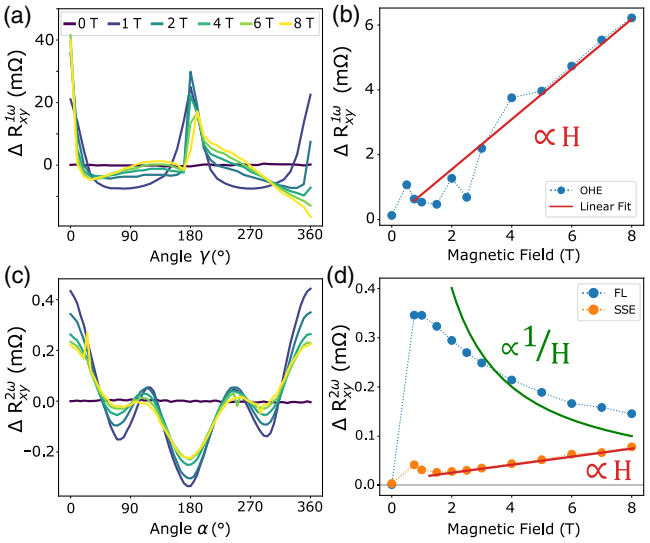

FIG. 3. Separating Hall effect and spin Seebeck effect contributions. (a) Field dependence of the first harmonic response in YZ scan, from 0 to 8 T as indicated by the legend. (b) The Hall effect in the first harmonic YZ scan (a), as a function of applied field. The linear trend line supports the claim that the origin of the signal is the ordinary Hall effect. (c) Field dependence of the second harmonic response in the XY scan, which shares the same legend as (a). (d) Antiferromagnetic spin Seebeck effect (SSE) separated from fieldlike SOT in the second harmonic XY scan (c), as a function of applied field. The fieldlike component scales as $1/H$, whereas the SSE component scales linearly with H.

Since the model assumes $|\boldsymbol{m}| \ll 1$, our solution breaks down at extremely large fields, which is partially reflected in Fig. 3 and discussed later.

The fieldlike torque and the dampinglike torque play very different roles in driving the dynamics of magnetic moments. As illustrated in Fig. 1(b), the dampinglike torque cants both magnetic moments towards the same in-plane direction, which will subsequently leverage the exchange torque between $\boldsymbol{m}_1$ and $\boldsymbol{m}_2$ so that the Néel vector $\boldsymbol{n}$ develops an out-of-plane component. By contrast, the fieldlike torque acts as an effective field that directly drives

the net magnetic moment so that the ac current induces an in-plane rotation of $\boldsymbol{m}$. Since $\boldsymbol{m}\perp\boldsymbol{n}$ by definition, a direct consequence is that $\boldsymbol{n}$ undergoes an in-plane oscillation. Correspondingly, in the absence of tilting, dampinglike torques vanish in the XY scan ($\theta_H = 90°$), and fieldlike torques vanish in the YZ scan ($\phi_H = 90°$). However, any amount of tilting of the easy plane will prevent this vanishing and both fieldlike and dampinglike torques will have contributions in XY and YZ scans.

Because of the small magnetic moment present in α-Fe_2O_3 above its Morin transition, perpendicular coupling between the Néel vector and the external field is easily achievable at moderate field strengths. The easy plane and the external field direction together are adequate to uniquely set the equilibrium direction of the Néel vector and a $\gtrsim$1 T in-plane component of the applied field can fully align the Néel vector to overcome any in-plane magnetic anisotropy.

We fit the experimental results with three free parameters: the direction of the hard axis ($\boldsymbol{e}_h$) and the amplitudes of the spin-orbit torques (H_{FL} and H_{DL}). For every scan, first we fit the first harmonic response, where we extract the current-independent constant R_0 [Eq. (4)]. Then together with the R_0, we use material parameters from the literature $H_D = 2$ T, $H_K = 0.01$ T, and $H_{\mathrm{ex}} = 900$ T [36–38], to fit the responses with our model. These fits allow us to extract the amplitudes of effective fields associated with the spin-orbit torques per current density which are $H_{\mathrm{FL}}/J_{\mathrm{ac}} \approx 7.5\times10^{-2}\,\mathrm{T}/(10^{12}\,\mathrm{A/m^2})$ and $H_{\mathrm{DL}}/J_{\mathrm{ac}} \approx 4.2\times10^{-4}\,\mathrm{T}/(10^{12}\,\mathrm{A/m^2})$.

A slight tilting ($\sim$3°) of the hard-axis $\boldsymbol{e}_h$ from the $\hat{z}$ direction is needed in order to simultaneously capture the form of each and every one of the field scans. This tilt is especially crucial in first harmonic out-of-plane scans (XZ and YZ), where in order to get any nonzero response from our model, we need some degree of canting of the easy plane. Moreover, to explain the shape of the response, an additional cosine term is needed, which we interpret as the ordinary Hall effect response of Pt.

There are thus effects arising from the ordinary Hall effect induced by the perpendicular field component and from the spin Seebeck effect (SSE) due to a thermal gradient in the $\hat{z}$ direction caused by Joule heating. Figure 3 summarizes how we extracted these contributions. On the left [Figs. 3(a) and 3(c)], we show the field dependence of first harmonic YZ and second harmonic XY scans. And, on the right [Figs. 3(b) and 3(d)], we show the separated contributions of the Hall effect and SSE from those scans, respectively. The field dependence of the signals can be used to isolate different contributions to the signal, as well as to show the model field dependence with the experimental results. Figure 3(b) shows the Hall effect contribution in first harmonic and YZ scans. Since the expected Hall contribution is in the form $R_H^{1\omega} = HR_0^H\cos\theta$, the linear trend with applied field supports our claim. Similarly, Fig. 3(d) shows decomposition of $R_{xy}^{2\omega}$ into two components: fieldlike SOT (blue) $R_{\mathrm{FL}}^{2\omega}$ and spin Seebeck effect (orange) $R_{\mathrm{SSE}}^{2\omega}$. In this case, the expected signals are of the form $R_{\mathrm{FL}}^{2\omega} = HR_0^{\mathrm{FL}}\cos 2\alpha\cos\alpha$ and $R_{\mathrm{SSE}}^{2\omega} = HR_0^{\mathrm{SSE}}\cos\alpha$ for fieldlike and SSE contributions, respectively. The form of the SSE contribution indicates that the effect is associated with the excess moment in the so called transverse spin Seebeck geometry, in which the signal scales linearly with the applied field [39]. Furthermore, the remaining fieldlike component decreases with increasing applied magnetic field and follows a $1/H$ dependence, as in Eq. (5). We attribute the deviation from a $1/H$ dependence at low and high fields to the fact that our model assumptions are not valid in those limits.

Our experimental results show that the fieldlike torque is about 2 orders of magnitude larger than the dampinglike torque, distinct from what is found in ferromagnets [40,41]. This implies that in the spin mixing conductance $g = g_r + ig_i$—which characterizes the spin transmission across the interface—the imaginary part g_i far exceeds the real part g_r, as $H_{\mathrm{DL}} \sim g_r J_{\mathrm{ac}}$ and $H_{\mathrm{FL}} \sim g_i J_{\mathrm{ac}}$ (see Supplemental Material [33]). To get at the origin of this unusual observation, we calculate g_i and g_r for a compensated interface by considering interfacial spin-dependent scattering processes, because electrons can deliver angular momenta to the magnetic moments near the interface

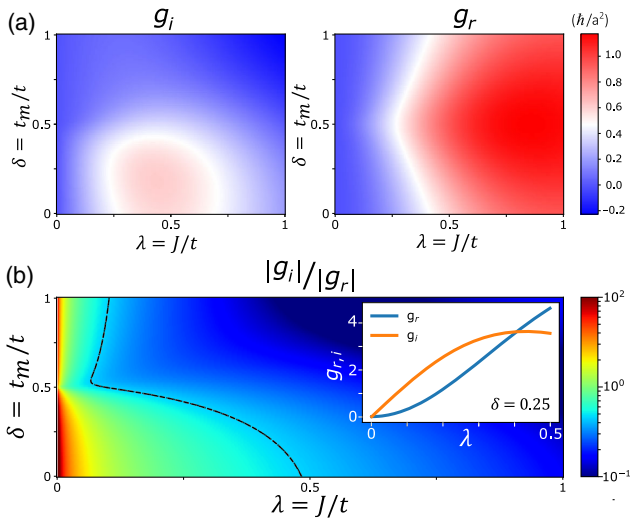

FIG. 4. (a) Imaginary (left) and real (right) parts of the spin mixing conductance ($g = g_r + ig_i$) of an AFM-NM interface. The scale is indicated by the shared color bar on the right, with units of $\hbar$ per unit area a^2 on the interface, where a is the lattice constant. (b) Ratio of $|g_i|$ to $|g_r|$. As λ approaches zero $|g_i|$ dominates over $|g_r|$. The dashed line shows $|g_i| = |g_r|$, which separates the fieldlike torque dominating region ($g_i > g_r$) on the left from the dampinglike torque dominating region ($g_r > g_i$) on the right. The color bar scale is logarithmic in this case. The inset shows a line cut of g_r and g_i vs λ at $\delta = 0.25$. Even though they both approach zero as λ goes to zero, g_r decreases faster than g_i and their ratio g_i/g_r diverges.

through spin-flip scattering [11,42], which manifests as spin torques exerting on the AFM. As detailed in Sec. 4 of the Supplemental Material [33], the interfacial scattering here depends on three parameters: the electron hopping energy t in the nonmagnet (NM) (determined by the Fermi energy), the proximity-induced hopping t_m on the AFM side of the interface [43], and the interfacial exchange coupling J between conduction electrons in the NM and the magnetic moments in the AFM. In Fig. 4 we plot the dependence of g_r and g_i on two dimensionless parameters $\lambda = J/t$ and $\delta = t_m/t$.

We see from Fig. 4 that regions with small λ and δ have $g_i/g_r > 1$. This ratio can become extremely large when λ becomes even smaller, which, when comparing with our experiment, indicates that the Pt/α-Fe_2O_3 interface just falls in the region of very small λ and δ. In general, the ratio g_i/g_r can vary over a wide range of values depending on λ and δ, thus it is expected that the relative strength of the fieldlike and dampinglike torques can vary significantly in different materials.

In conclusion, we determined the type and amplitude of SOTs in antiferromagnetic α-Fe_2O_3/Pt bilayers. An important finding is that the fieldlike torques are 2 orders of magnitude larger than dampinglike torques, implying that the spin-mixing conductance of the α-Fe_2O_3/Pt interface has the unusual property of having a large imaginary component. It also points to magnetoelastic effects likely being the dominant mechanism of current-induced switching of the Néel vector of α-Fe_2O_3 [8,9,28]. In fact, third harmonic measurements have shown that magnetoelastic effects can be as important as dampinglike torques at higher current amplitudes [44]. Our method can be extended to other AFM-HM systems by starting with the appropriate model and assumptions (e.g., magnetic anisotropies, DMI) to determine harmonic response [35]. Overall, our work demonstrates a way to quantify SOTs and opens up a promising path for future studies on similar AFM-HM heterostructures as well as a means that can be used in optimizing SOTs on AFM for applications.

This research was supported by the Air Force Office of Scientific Research under Grant No. FA9550-19-1-0307 and, in part, by the National Science Foundation under Grant No. NSF-DMR-2105114. The nanostructures were realized at the Advanced Science Research Center NanoFabrication Facility of the Graduate Center at the City University of New York.

[1] E. V. Gomonay and V. M. Loktev, Spintronics of antiferromagnetic systems (Review Article), Low Temp. Phys. **40**, 17 (2014).

[2] T. Jungwirth, X. Marti, P. Wadley, and J. Wunderlich, Antiferromagnetic spintronics, Nat. Nanotechnol. **11**, 231 (2016).

[3] V. Baltz, A. Manchon, M. Tsoi, T. Moriyama, T. Ono, and Y. Tserkovnyak, Antiferromagnetic spintronics, Rev. Mod. Phys. **90**, 015005 (2018).

[4] S. Fukami, V. O. Lorenz, and O. Gomonay, Antiferromagnetic spintronics, J. Appl. Phys. **128**, 070401 (2020).

[5] P. Wadley *et al.*, Electrical switching of an antiferromagnet, Science **351**, 587 (2016).

[6] R. Cheng, D. Xiao, and A. Brataas, Terahertz Antiferromagnetic Spin Hall Nano-Oscillator, Phys. Rev. Lett. **116**, 207603 (2016).

[7] I. Gray, T. Moriyama, N. Sivadas, G. M. Stiehl, J. T. Heron, R. Need, B. J. Kirby, D. H. Low, K. C. Nowack, D. G. Schlom, D. C. Ralph, T. Ono, and G. D. Fuchs, Spin Seebeck Imaging of Spin-Torque Switching in Antiferromagnetic Pt/NiO Heterostructures, Phys. Rev. X **9**, 041016 (2019).

[8] Y. Cheng, S. Yu, M. Zhu, J. Hwang, and F. Yang, Electrical Switching of Tristate Antiferromagnetic Néel Order in α-Fe_2O_3 Epitaxial Films, Phys. Rev. Lett. **124**, 027202 (2020).

[9] E. Cogulu, N. N. Statuto, Y. Cheng, F. Yang, R. V. Chopdekar, H. Ohldag, and A. D. Kent, Direct imaging of electrical switching of antiferromagnetic Néel order in α-Fe_2O_3 epitaxial films, Phys. Rev. B **103**, L100405 (2021).

[10] H. V. Gomonay and V. M. Loktev, Spin transfer and current-induced switching in antiferromagnets, Phys. Rev. B **81**, 144427 (2010).

[11] R. Cheng, J. Xiao, Q. Niu, and A. Brataas, Spin Pumping and Spin-Transfer Torques in Antiferromagnets, Phys. Rev. Lett. **113**, 057601 (2014).

[12] C. O. Avci, K. Garello, M. Gabureac, A. Ghosh, A. Fuhrer, S. F. Alvarado, and P. Gambardella, Interplay of spin-orbit torque and thermoelectric effects in ferromagnet/normal-metal bilayers, Phys. Rev. B **90**, 224427 (2014).

[13] S. Y. Bodnar, L. Šmejkal, I. Turek, T. Jungwirth, O. Gomonay, J. Sinova, A. A. Sapozhnik, H.-J. Elmers, M. Kläui, and M. Jourdan, Writing and reading antiferromagnetic Mn_2Au by Néel spin-orbit torques and large anisotropic magnetoresistance, Nat. Commun. **9**, 348 (2018).

[14] X. Z. Chen, R. Zarzuela, J. Zhang, C. Song, X. F. Zhou, G. Y. Shi, F. Li, H. A. Zhou, W. J. Jiang, F. Pan, and Y. Tserkovnyak, Antidamping-Torque-Induced Switching in Biaxial Antiferromagnetic Insulators, Phys. Rev. Lett. **120**, 207204 (2018).

[15] X. F. Zhou, J. Zhang, F. Li, X. Z. Chen, G. Y. Shi, Y. Z. Tan, Y. D. Gu, M. S. Saleem, H. Q. Wu, F. Pan, and C. Song, Strong Orientation-Dependent Spin-Orbit Torque in Thin Films of the Antiferromagnet Mn_2Au, Phys. Rev. Applied **9**, 054028 (2018).

[16] A. Parthasarathy, E. Cogulu, A. D. Kent, and S. Rakheja, Precessional spin-torque dynamics in biaxial antiferromagnets, Phys. Rev. B **103**, 024450 (2021).

[17] Q. Shao, P. Li, L. Liu, H. Yang, S. Fukami, A. Razavi, H. Wu, K. Wang, F. Freimuth, Y. Mokrousov, M. D. Stiles, S. Emori, A. Hoffmann, J. Akerman, K. Roy, J.-P. Wang, S.-H. Yang, K. Garello, and W. Zhang, Roadmap of spin–orbit torques, IEEE Trans. Magn. **57**, 1 (2021).

[18] L. Zhu, D. C. Ralph, and R. A. Buhrman, Maximizing spin-orbit torque generated by the spin Hall effect of Pt, Appl. Phys. Rev. **8**, 031308 (2021).

[19] L. Baldrati, A. Ross, T. Niizeki, C. Schneider, R. Ramos, J. Cramer, O. Gomonay, M. Filianina, T. Savchenko, D. Heinze, A. Kleibert, E. Saitoh, J. Sinova, and M. Kläui, Full angular dependence of the spin Hall and ordinary magnetoresistance in epitaxial antiferromagnetic NiO(001)/Pt thin films, Phys. Rev. B **98**, 024422 (2018).

[20] Y. Cheng, S. Yu, A. S. Ahmed, M. Zhu, Y. Rao, M. Ghazisaeidi, J. Hwang, and F. Yang, Anisotropic magnetoresistance and nontrivial spin Hall magnetoresistance in Pt/α-Fe_2O_3 bilayers, Phys. Rev. B **100**, 220408(R) (2019).

[21] J. E. Hirsch, Spin Hall Effect, Phys. Rev. Lett. **83**, 1834 (1999).

[22] G. Y. Guo, S. Murakami, T.-W. Chen, and N. Nagaosa, Intrinsic Spin Hall Effect in Platinum: First-Principles Calculations, Phys. Rev. Lett. **100**, 096401 (2008).

[23] H. Nakayama, M. Althammer, Y.-T. Chen, K. Uchida, Y. Kajiwara, D. Kikuchi, T. Ohtani, S. Geprägs, M. Opel, S. Takahashi, R. Gross, G. E. W. Bauer, S. T. B. Goennenwein, and E. Saitoh, Spin Hall Magnetoresistance Induced by a Nonequilibrium Proximity Effect, Phys. Rev. Lett. **110**, 206601 (2013).

[24] G. R. Hoogeboom, A. Aqeel, T. Kuschel, T. T. M. Palstra, and B. J. van Wees, Negative spin hall magnetoresistance of pt on the bulk easy-plane antiferromagnet NiO, Appl. Phys. Lett. **111**, 052409 (2017).

[25] Y.-T. Chen, S. Takahashi, H. Nakayama, M. Althammer, S. T. B. Goennenwein, E. Saitoh, and G. E. W. Bauer, Theory of spin Hall magnetoresistance, Phys. Rev. B **87**, 144411 (2013).

[26] T. Taniguchi, J. Grollier, and M. D. Stiles, Spin-Transfer Torques Generated by the Anomalous Hall Effect and Anisotropic Magnetoresistance, Phys. Rev. Applied **3**, 044001 (2015).

[27] C. Schmitt, L. Baldrati, L. Sanchez-Tejerina, F. Schreiber, A. Ross, M. Filianina, S. Ding, F. Fuhrmann, R. Ramos, F. Maccherozzi, D. Backes, M.-A. Mawass, F. Kronast, S. Valencia, E. Saitoh, G. Finocchio, and M. Kläui, Identification of Néel Vector Orientation in Antiferromagnetic Domains Switched by Currents in NiO/Pt Thin Films, Phys. Rev. Applied **15**, 034047 (2021).

[28] P. Zhang, J. Finley, T. Safi, and L. Liu, Quantitative Study on Current-Induced Effect in an Antiferromagnet Insulator/Pt Bilayer Film, Phys. Rev. Lett. **123**, 247206 (2019).

[29] M. Hayashi, J. Kim, M. Yamanouchi, and H. Ohno, Quantitative characterization of the spin-orbit torque using harmonic Hall voltage measurements, Phys. Rev. B **89**, 144425 (2014).

[30] J. Fischer, O. Gomonay, R. Schlitz, K. Ganzhorn, N. Vlietstra, M. Althammer, H. Huebl, M. Opel, R. Gross, S. T. B. Goennenwein, and S. Geprägs, Spin Hall magnetoresistance in antiferromagnet/heavy-metal heterostructures, Phys. Rev. B **97**, 014417 (2018).

[31] R. Lebrun, A. Ross, O. Gomonay, S. A. Bender, L. Baldrati, F. Kronast, A. Qaiumzadeh, J. Sinova, A. Brataas, R. A. Duine, and M. Kläui, Anisotropies and magnetic phase transitions in insulating antiferromagnets determined by a Spin-Hall magnetoresistance probe, Commun. Phys. **2**, 50 (2019).

[32] We note that contribution to R_{xy} of the form $m_x m_y$ is negligible.

[33] See Supplemental Material at http://link.aps.org/supplemental/10.1103/PhysRevLett.128.247204 for the full harmonic Hall data set, computation of the current-induced Oersted fields and the calculation of the spin-mixing conductance.

[34] M. Seavey, Acoustic resonance in the easy-plane weak ferromagnets α-Fe_2O_3 and $FeBO_3$, Solid State Commun. **10**, 219 (1972).

[35] H. Zhang and R. Cheng, Theory of harmonic Hall responses of spin-torque driven antiferromagnets, J. Magn. Magn. Mater. **556**, 169362 (2022).

[36] S. J. Williamson and S. Foner, Antiferromagnetic resonance in systems with Dzyaloshinsky-Moriya coupling; orientation dependence in α-Fe_2O_3, Phys. Rev. **136**, A1102 (1964).

[37] K. Mizushima and S. Iida, Effective in-plane anisotropy field in α-Fe_2O_3, J. Phys. Soc. Jpn. **21**, 1521 (1966).

[38] P. R. Elliston and G. J. Troup, Some antiferromagnetic resonance measurements in α-Fe_2O_3, J. Phys. C **1**, 169 (1968).

[39] G. E. W. Bauer, E. Saitoh, and B. J. van Wees, Spin caloritronics, Nat. Mater. **11**, 391 (2012).

[40] Y. Tserkovnyak, A. Brataas, and G. E. W. Bauer, Spin pumping and magnetization dynamics in metallic multilayers, Phys. Rev. B **66**, 224403 (2002).

[41] K. Xia, P. J. Kelly, G. Bauer, A. Brataas, and I. Turek, Spin torques in ferromagnetic/normal-metal structures, Phys. Rev. B **65**, 220401(R) (2002).

[42] R. Cheng, Aspects of antiferromagnetic spintronics, Ph.D. thesis, The University of Texas at Austin, 2014, http://hdl.handle.net/2152/25928.

[43] In AFMs, the spin and sublattice degrees of freedom are locked together. Therefore, a spin-flip scattering must involve electron hopping between the two sublattices on the AFM side of the interface. Since the AFM is insulating by itself, such a process must rely on the proximity-induced t_m.

[44] Y. Cheng, E. Cogulu, R. D. Resnick, J. J. Michel, N. N. Statuto, A. D. Kent, and F. Yang, Third harmonic characterization of antiferromagnetic heterostructures, arXiv:2112.13159.